Photon-trapping-enhanced avalanche photodiodes for mid-infrared applications

Dekang Chen [1], Stephen D. March [2], Andrew H. Jones [1], Yang Shen [1], Adam A. Dadey [1], Keye Sun[1], J. Andrew McArthur [2], Alec M. Skipper [2], Xingjun Xue[1], Bingtian Guo[1], Junwu Bai [1], Seth R. Bank [2] & Joe C. Campbell [1] ✉

The fast development of mid-wave infrared photonics has increased the demand for high-performance photodetectors that operate in this spectral range. However, the signal-to-noise ratio, regarded as a primary figure of merit for mid-wave infrared detection, is strongly limited by the high dark current in narrow-bandgap materials. Therefore, conventional mid-wave infrared photodetectors such as HgCdTe require cryogenic temperatures to avoid excessively high dark current. To address this challenge, we report an avalanche photodiode design using photon-trapping structures to enhance the quantum efficiency and minimize the absorber thickness to suppress the dark current. The device exhibits high quantum efficiency and dark current density that is nearly three orders of magnitude lower than that of the state-of-the-art HgCdTe avalanche photodiodes and nearly two orders lower than that of previously reported AlInAsSb avalanche photodiodes that operate at 2 µm. Additionally, the bandwidth of these avalanche photodiodes reaches ~7 GHz, and the gain–bandwidth product is over 200 GHz; both are more than four times those of previously reported 2 µm avalanche photodiodes.

Mid-wave infrared (MWIR) photonics, typically referring to the wavelength range of 2–5 µm, has the potential to enable next-generation breakthroughs in a wide area of applications, including sensing[1], spectroscopy[2,3], medical diagnostics[4,5] and communications[6]. Recently, MWIR devices were successfully integrated into silicon platforms to realize MWIR silicon photonics[7], which substantially expands the application scope of MWIR photonics. As a key receiver component in a photonic system, there is escalating interest in high-performance MWIR photodetectors.

For applications in the MWIR range, a primary figure of merit is the signal-to-noise ratio (SNR), defined as the ratio between the signal and noise powers. However, improving the SNR performance of MWIR photodetectors is very challenging due to the weak signal power for many applications in the MWIR range. Imaging and sensing require the detection of signals from a long distance through free space, meaning the optical signal that reaches the photodetector is usually weak and, in some instances, may reach the few-photons level. Consequently, avalanche photodiodes (APDs) are attractive for MWIR detection owing to their low-noise internal gain, which can amplify the weak optical signal above the thermal and circuit noise, resulting in improved SNR. However, APDs also boost the shot noise current due to the random nature of the impact ionization process, referred to as the excess noise, which can degrade the SNR. However, in addition to the excess noise, in the MWIR range, APDs can also suffer from detrimentally high dark current. Narrow-bandgap materials used to absorb the mid-wave optical signal, such as HgCdTe (ref. 8), InAs/GaSb type-II superlattice (T2SL) (ref. 9) and InAs/InAsSb type-II strained-layer superlattice (T2SLS) (ref. 10), are typically a source of high dark current due to the Shockley–Read–Hall generation, tunnelling or even thermal generation over the narrow bandgap. Therefore,

[1]Department of Electrical and Computer Engineering, University of Virginia, Charlottesville, VA, USA. [2]Microelectronics Research Center, University of Texas, Austin, TX, USA. ✉e-mail: jcc7s@virginia.edu
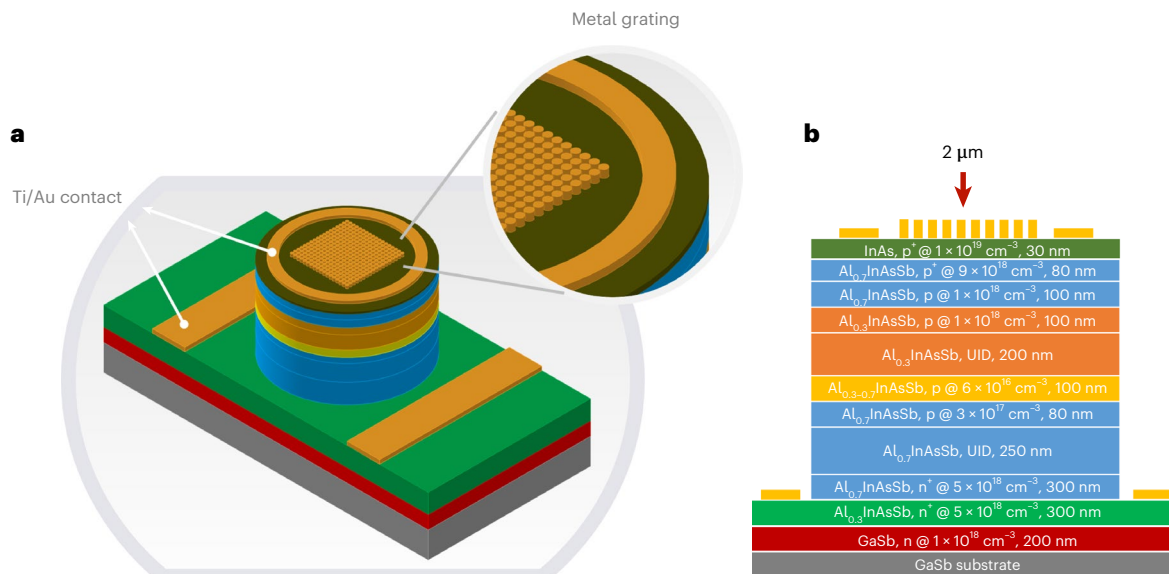
Fig. 1 | Photon-trapping SACM APD structure. a, Schematic view. **b**, Cross-sectional view of the epitaxial layer structure. From the top of the device, the compositions of the layer material are listed as follows: (1) InAs cap layer, p+, 1×10^{19} cm^{-3}; (2) Al$_{0.7}$InAsSb contact layer, p+, 9×10^{18} cm^{-3}; (3) Al$_{0.7}$InAsSb blocking layer, p, 1×10^{18} cm^{-3}; (4) Al$_{0.3}$InAsSb blocking layer, p, 1×10^{18} cm^{-3}; (5) Al$_{0.3}$InAsSb absorber, UID; (6) Al$_{0.3-0.7}$InAsSb bandgap grading layer, p, 6×10^{16} cm^{-3}; (7) Al$_{0.7}$InAsSb charge layer, p, 3×10^{17} cm^{-3}; (8) Al$_{0.7}$InAsSb multiplication layer, UID; (9) Al$_{0.7}$InAsSb contact layer, n+, 5×10^{18} cm^{-3}; (10) Al$_{0.3}$InAsSb contact layer, n+, 5×10^{18} cm^{-3}; (11) GaSb buffer layer, n, 1×10^{18} cm^{-3}; (12) GaSb substrate.

conventional MWIR photodetectors, such as HgCdTe photodetectors[8], need to be cooled to cryogenic temperatures to avoid excessively high dark current. This adds to the cost, complicates packaging and system design, and limits the mobile application space. Therefore, reducing the dark current of MWIR APDs is a necessary challenge for improving the device performance.

Recently, we demonstrated the first 2 µm separate absorption, charge and multiplication (SACM) APDs[11] based on the digital alloy Al$_x$In$_{1-x}$As$_y$Sb$_{1-y}$ materials system[12] and achieved comparable dark current with a HgCdTe APD at nearly 100 K higher operating temperature. One approach to further improve the SNR is to reduce the dark current. Since the primary source of dark current is the narrow-bandgap absorber, one of the most straightforward solutions is to reduce its thickness. A thinner absorber, however, reduces the photon absorption and quantum efficiency, which degrades the SNR. Therefore, the goal is to maintain a high quantum efficiency within an ultrathin absorber, and one of the most effective approaches to achieve this is to use photon-trapping structures, such as photonic crystals[13–15] or metal plasmonic structures[16,17]. To date, these approaches have not been demonstrated for MWIR APDs. Recently, we proposed a photon-trapping approach to improve the quantum efficiency of an SACM APD with an ultrathin absorber using submicrometre metal grating arrays[18]. The simulation showed that the quantum efficiency can be increased more than four times that of a planar surface. This enhancement comes from diffracting and coupling normal-incident light into the laterally propagating mode inside the absorber. In this work, we describe the design and experimentally demonstrate the first photon-trapping-enhanced 2 µm APDs.

Design

A schematic of the photon-trapping SACM APD and a cross-section schematic of the epitaxial layers are shown in Fig. 1a,b, respectively. A narrow-bandgap Al$_{0.3}$InAsSb layer ($E_g \approx 0.58$ eV) is used to achieve efficient absorption at 2 µm. The thickness of the unintentionally doped (UID) absorber has been reduced to 200 nm to suppress the dark current from the narrow bandgap and still support a waveguide mode in the absorber to enable the photon-trapping mechanism

of the structure[18]. Wide-bandgap Al$_{0.7}$InAsSb ($E_g \approx 1.16$ eV) is used as the multiplication layer. As an APD, this material has been shown to exhibit low dark current, high gain and excess noise comparable with that of Si (ref. 11). The thickness of the multiplication layer has been designed to maximize the gain–bandwidth product, accounting for the thickness tradeoff between a high maximum gain and a high gain–bandwidth product. A critical consideration for SACM APDs is the charge layer, which is designed to provide sufficient electric-field contrast between the absorber and multiplication region. This helps avoid early device breakdown and maintain a moderate punch-through bias. An Al$_{0.3-0.7}$InAsSb grading layer with continuously graded Al composition is used to provide a smooth bandgap variation from the absorber to the multiplication region. This facilitates efficient electron injection and enables a high transit-time bandwidth.

To maintain high quantum efficiency within the ultrathin absorber, photon-trapping structures using two-dimensional rectangular lattice were incorporated with metal grating arrays on top of the device (Fig. 2a). With the optimized grating dimensions (spacing, 598 nm; duty cycle, 0.82; thickness, 380 nm) (Fig. 2b), the external quantum efficiency (EQE) can be theoretically increased to ~36%, which is nearly five times that of the planar surface (Fig. 2c). The mechanism for absorption enhancement is twofold. First, the narrow-bandgap Al$_{0.3}$InAsSb absorber has a higher refractive index than the surrounding wide-bandgap layers, and therefore, waveguide modes are supported in the absorber. When normal-incidence light reaches the periodic grating arrays, it is diffracted and can laterally couple into the waveguide modes in the absorber, that is, the absorption is enhanced by photon trapping. The distribution of the magnetic-field profile is simulated and plotted (Fig. 2d), which indicates strong field confinement inside the absorber. The other enhancement comes from the plasmon-enhanced transmission effect[19–21] and near-field diffraction characteristic of the metal grating[22,23]. This can enhance the efficiency of the lateral coupling process, making it more efficient than using a dielectric grating or photonic crystal[18]. More details regarding the photon-trapping mechanism of the photon-trapping structure are discussed in our previous theoretical work[18].
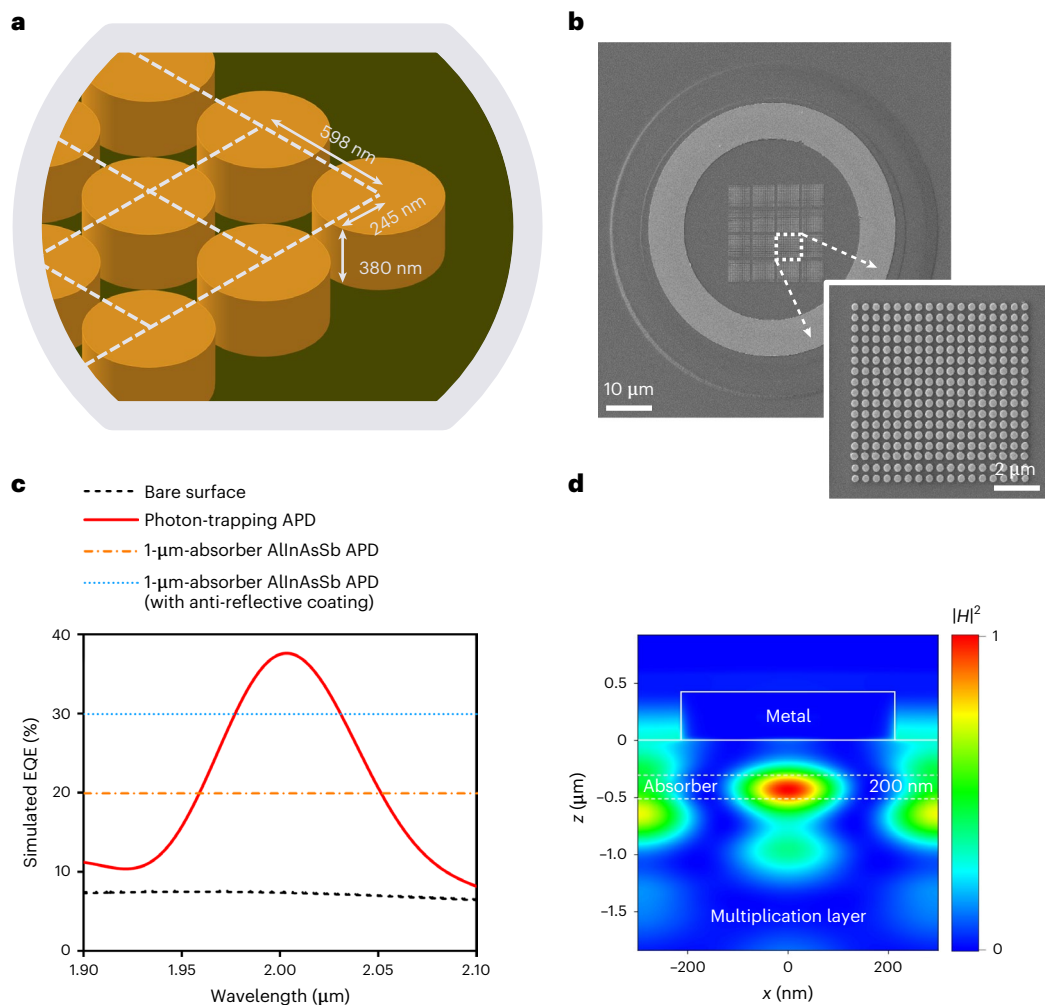
Fig. 2 | Details of the metal grating array. a, Designed dimensions. **b**, Scanning electron microscopy image of the fabricated photon-trapping SACM APD. The inset shows a high-magnification view of the grating region. **c**, Simulated EQE of the photon-trapping SACM APD with the designed grating dimensions; the dashed lines show the EQE of the first 2 µm AlInAsSb SACM APD with a 1-µm-thick absorber[11]. **d**, Normalized distribution of the square of the magnetic-field intensity $|H|^2$ at the cross section of the device. The region between the two dashed lines represents the 200-nm-thick $Al_{0.3}InAsSb$ layer.

Experiment

The designed layer structure (Fig. 1b) was grown by molecular-beam epitaxy as a digital alloy lattice matched to an n-type GaSb substrate comprising four binaries: AlAs, AlSb, InAs and InSb. The wafer was fabricated into circular mesa structures by standard photolithography techniques and citric acid wet etching. Finally, submicrometre metal grating arrays were fabricated on top of the mesa by electron-beam lithography and metal lift-off process. It is worth noting that the metal was deposited as a stack of 10 nm Ti and 370 nm Au, where the Ti layer is used to improve adhesion between Au and the semiconductor. A scanning electron microscopy image of the fabricated photon-trapping SACM APD is shown in Fig. 2a. The performance of these APDs is characterized as follows.

Gain and noise

Figure 3a shows the room-temperature current–voltage (I–V) curves of a 100-µm-diameter device under 2 µm laser illumination. The photocurrent punch-through occurs at almost −16 V, indicating the extension of the electric field into the absorber, and the photogenerated carriers begin to be injected into the multiplication layer. Before calculating the gain, it is worth noting that at the punch-through voltage, the gain is not necessarily unity and needs to be fitted by the excess noise measurement. Details regarding the fitting method can be found

elsewhere[24]. After fitting with the excess noise measurement, the gain at the punch-through voltage (−16 V) was determined to be ~4. Therefore, the absolute gain of the device at a voltage above punch-through can be calculated by multiplying the relative gain at that voltage compared with the signal at −16 V by the fitted gain at punch-through, i.e., 4. The calculated absolute-gain curve is plotted in Fig. 3a (right vertical axis). To explore the maximum gain level of the device, the gain curve was also measured at 240 K to reduce the dark current and using high optical attenuation to minimize the gain saturation effect. As shown in Fig. 3b, the maximum gain of the device approaches ~700 at 240 K with low optical intensity (~10 nW). To the best of our knowledge, this is the highest demonstrated gain for 2 µm APDs using III–V semiconductors.

Although the SNR of the photon-trapping SACM APD benefits from its high gain, the shot noise current is also amplified[25]:

$$I^2_{shot} = 2qM^2 \left(I_{photo} + I_{dark} \right) F(M) \Delta f, \tag{1}$$

where q is the electron charge; M is the multiplication gain; $F(M)$ is the excess noise factor; Δf is the operating bandwidth; and I_{photo} and I_{dark} are the photocurrent and dark current, respectively. The excess noise factor $F(M)$ is expressed as[25]:

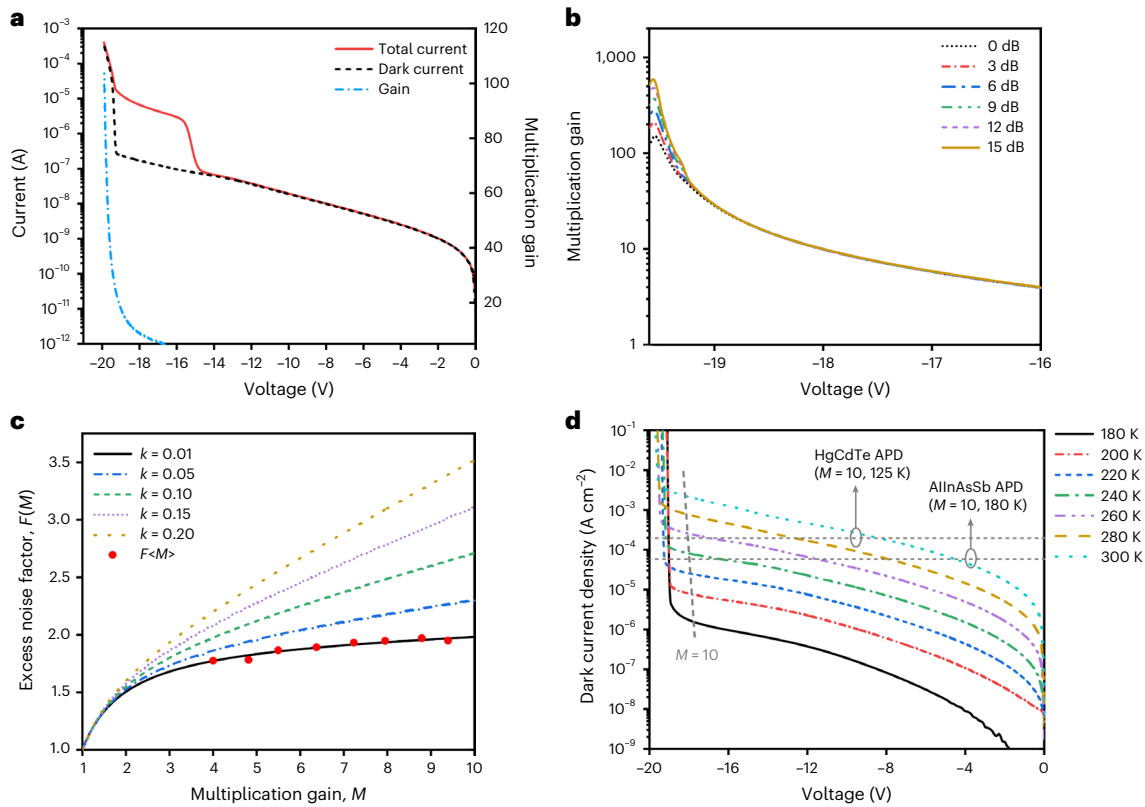$$F(M) = kM + (1-k)\left(2 - \frac{1}{M}\right), \tag{2}$$

Fig. 3 | Current–voltage, measured gain and excess noise measurements.
a, Measured current–voltage and gain curves of a 100-μm-diameter device at room temperature. **b**, Measured gain curves of the device at 240 K with different optical attenuations. **c**, Measured excess noise factors of the device under 2 μm illumination; the solid line shows the theoretical excess noise factors for k values from 0.01 to 0.20. **d**, Measured dark current density at various temperatures; the dark current densities of the state-of-the-art 2 μm HgCdTe APD[8] and AlInAsSb APD[11] are plotted for reference.

where M is the gain and k is the ratio of the electron (α) and hole (β) impact ionization coefficients. To characterize the excess noise of the device, the excess noise factor $F(M)$ as a function of multiplication gain M is measured and plotted (Fig. 3c). The theoretical excess noise factors for k values from 0.01 to 0.20 were also calculated using the local-field model[25]. Under 2 μm illumination, the measured k value of the device is approximately 0.01, consistent with previously reported AlInAsSb APDs[11,26]. This value is extremely low compared with conventional III–V semiconductor APDs and is comparable with that of silicon APDs[27].

Dark current

As discussed above, dark current is one of the primary noise sources in MWIR APDs due to the narrow-bandgap material. It substantially contributes to the total shot noise of the device, as indicated by equation (1). To evaluate the dark current performance, temperature-dependent dark current density was measured (Fig. 3d). The references (Fig. 3d, dashed lines) to a state-of-the-art HgCdTe APD[8] and AlInAsSb APD[11] are also included for comparison. It is evident that at the same temperature, the dark current density of the thin absorber is nearly two orders lower than the AlInAsSb APD with a 1-μm-thick absorber and nearly three orders lower than the state-of-the-art HgCdTe APD[8].

Quantum efficiency

Although the thin-absorber-based SACM APD shows high gain and low noise due to the largely suppressed dark current and low k value, the ultrathin absorber results in low quantum efficiency and reduced SNR. To verify this, the EQE of the device was measured under surface-normal illumination using a 2 μm semiconductor laser. The result shows that although the EQE of the planar surface device is ~7% at 2 μm, the photon-trapping-enhanced device shows EQE of ~22%.
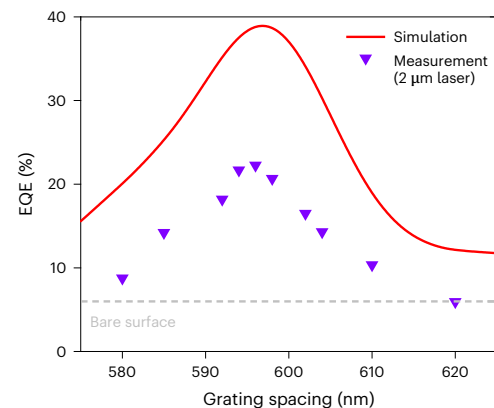

Fig. 4 | EQE for different grating spacings. Measured EQE of the photon-trapping SACM APD versus grating spacing.

Although the measured efficiency is still lower than the simulated value of ~38%, the achieved 22% EQE is more than three times that of the bare surface device and is even 2% higher than the previously reported EQE of the 2 μm SACM APD with a 1-μm-thick absorber[11]. The difference between the measured and simulated EQE is primarily caused by fabrication limitations, including the metal thickness, pattern shape, sidewall bevel angles and possible oxidization of the Ti adhesion layer. Together with lower dark current provided by the ultrathin absorber design, the SNR of the photon-trapping SACM APD could reach ~70 times that of the first 2 μm AlInAsSb SACM APDs[11] and ~20 times that of the state-of-the-art HgCdTe APD[8] under low optical
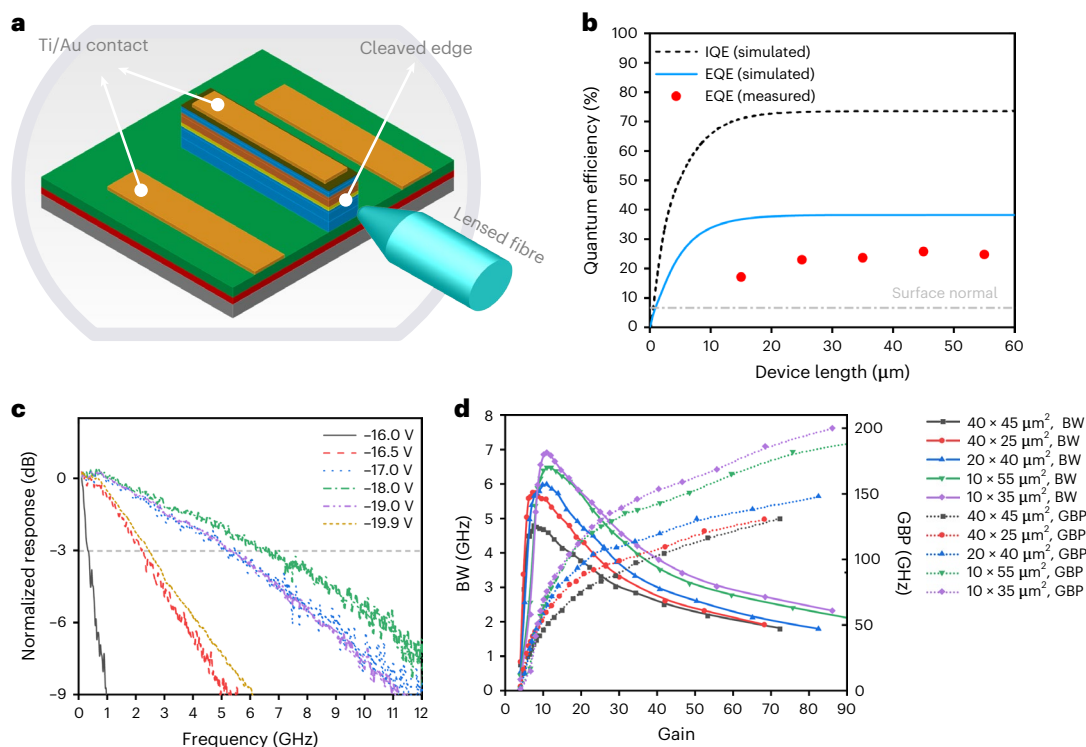
Fig. 5 | EQE and bandwidth of the edge-coupled waveguide APD. a, Schematic of the edge-coupled waveguide APD. **b**, Measured EQE of the edge-coupled waveguide APD at 2 μm; the simulated result is plotted for reference.

c, Frequency response of the SACM APD with dimensions of $10 \times 35\ \mu m^2$.
d, Summary of the measured bandwidth (BW) and gain–bandwidth product (GBP) of the SACM APDs with different dimensions.

Table 1 | Major performance parameters of photon-trapping APDs in this work, AlInAsSb APDs and state-of-the-art HgCdTe APDs at 2 μm

Device	J_{dark}	Gain	EQE	Bandwidth	Gain–bandwidth product
Present work	1×10^{-6} A cm^{-2} (180 K)	~700	~22%	~7 GHz	~200 GHz
2 μm AlInAsSb APD[11]	6×10^{-5} A cm^{-2} (180 K)	~200	~20%	~1.5 GHz	~44 GHz
2 μm HgCdTe APD[8]	2×10^{-4} A cm^{-2} (125 K)	~1,000	~75%	Not reported	Not reported

intensity. More details about the SNR calculation and comparison are provided in the Supplementary Information.

To further investigate the absorption enhancement mechanism of the photon-trapping structure, the EQE was measured with different grating spacings, and the result is shown in Fig. 4. It is clear that the measured efficiency decreases when the spacing differs from the optimum value of 596 nm, which follows the trend predicted by the simulation. This result is consistent with the analysis done elsewhere[18], that is, photon trapping functions as a grating coupler, and therefore, the peak wavelength and grating spacing comply with the Bragg condition.

Since one of the enhancement mechanisms of the photon-trapping structure is lateral coupling, an alternative solution is coupling to the absorber waveguide through the edge of the device (Fig. 5a). The edge-coupling approach can be highly efficient, and moreover, it may be more compatible with applications such as a fibre array packaged device or a photonic integrated circuit. Figure 5b shows the simulated internal quantum efficiency (IQE), simulated EQE and the measured EQE of waveguide devices using a lensed fibre to couple into the cleaved

edge. More details about the measurement steps and calibration are included in the Supplementary Information. The results show that the EQE quickly saturates with the waveguide length after ~20 μm, as expected in the simulation, and finally reaches ~24%, which is comparable with the photon-trapping approach. Since there is no anti-reflective coating on the edge, the EQE could be further improved to ~35% (ref. 18).

Bandwidth

In addition to suppressing the dark current to improve the SNR, another aspect of the ultrathin absorber design is to achieve high transit-time bandwidth. A high-speed device is possible using a small device area to provide high RC time bandwidth. Figure 5c shows the frequency response curves of a 10 μm × 35 μm device at various bias voltages. The extracted 3 dB bandwidth and gain–bandwidth product of the devices with different dimensions are summarized in Fig. 5d. For each device, the bandwidth first increases with the gain, peaks at ~10 and then starts to decrease. The increase in bandwidth before a gain value of 10 is due to insufficient voltage to fully deplete the absorber at punch-through. The decrease in bandwidth at higher gain is caused by the avalanche build-up time. Nevertheless, the gain–bandwidth product keeps increasing after $M \approx 10$ and then saturates. As shown in Fig. 5d (purple curve), the 10 μm × 35 μm device reaches a maximum 3 dB bandwidth of ~7 GHz and a gain–bandwidth product of over 200 GHz. As shown in Table 1, both these values are more than four times those of the previous record bandwidth for a 2 μm APD[28].

The measured bandwidth of the devices showed a clear area dependence, which may indicate an RC time bandwidth limit. To further understand the bandwidth limit, microwave scattering parameters (S_{11}) were measured and fitted to the equivalent circuit model of a photodiode to calculate the theoretical bandwidth. The result shows that the theoretical RC time bandwidth is 55.9 GHz for the 10 μm × 35 μm device, which is much higher than the measured 3 dB bandwidth. If no other bandwidth component exists, the transit-time bandwidth has to be less

than 10 GHz, which is much lower than the simulated value of ~31 GHz. The additional factor is attributed to the conductive GaSb substate. As reported elsewhere[29], a highly doped substrate can cause severe RF loss at high frequency and substantially limit the device speed. Nevertheless, by growing the device on a semi-insulating InP substrate in the future, the bandwidth of the device can be substantially improved, offering the potential to reach over 30 GHz.

Conclusion

We report a new MWIR SACM APD design with an ultrathin absorber to suppress dark current without sacrificing quantum efficiency by using photon-trapping structures. The device exhibits extremely low dark current, nearly two orders lower than the first 2 µm AlInAsSb APDs and nearly three orders lower than the state-of-the-art HgCdTe APDs. At the same time, the quantum efficiency reaches ~22% by using a photon-trapping structure and ~24% through edge coupling. Moreover, the maximum gain of the device is as high as ~700 at 240 K. Consequently, the SNR is improved more than 70 times that of the first 2 µm AlInAsSb APDs and nearly 20 times that of the state-of-the-art HgCdTe APD under low optical intensity. Additionally, the thin absorber design also enabled improved bandwidth. The frequency response measurement shows that the maximum bandwidth reaches ~7 GHz, and the gain–bandwidth product is over 200 GHz. Both these values are more than four times those previously reported for 2 µm APDs (Table 1). In addition to the performance improvement, this is also—to the best of our knowledge—the first time that photon-trapping structures are demonstrated on an APD. This idea breaks the low dark current and high-efficiency performance tradeoff for the detection of low-level signals in the MWIR regime, which could be further applied to a longer-wavelength-cutoff APD in the future.

Online content

Any methods, additional references, Nature Portfolio reporting summaries, source data, extended data, supplementary information, acknowledgements, peer review information; details of author contributions and competing interests; and statements of data and code availability are available at https://doi.org/10.1038/s41566-023-01208-x.

References

1. Willer, U., Saraji, M., Khorsandi, A., Geiser, P. & Schade, W. Near- and mid-infrared laser monitoring of industrial processes, environment and security applications. *Opt. Lasers Eng.* **44**, 699–710 (2006).
2. Rodrigo, D. et al. Mid-infrared plasmonic biosensing with graphene. *Science* **349**, 165–168 (2015).
3. Torkestani, S. S., Sahuguede, S., Julien-Vergonjanne, A. & Cances, J. P. Indoor optical wireless system dedicated to healthcare application in a hospital. *IET Commun.* **6**, 541–547 (2012).
4. Hugi, A., Villares, G., Blaser, S., Liu, H. C. & Faist, J. Mid-infrared frequency comb based on a quantum cascade laser. *Nature* **492**, 229–233 (2012).
5. Villares, G., Hugi, A., Blaser, S. & Faist, J. Dual-comb spectroscopy based on quantum-cascade-laser frequency combs. *Nat. Commun.* **5**, 5192 (2014).
6. Fang, B. et al. Bidirectional mid-infrared communications between two identical macroscopic graphene fibres. *Nat. Commun.* **11**, 6368 (2020).
7. Zou, Y., Chakravarty, S., Chung, C. J., Xu, X. C. & Chen, R. T. Mid-infrared silicon photonic waveguides and devices [Invited]. *Photon. Res.* **6**, 254–276 (2018).
8. Gravrand, O. et al. HgCdTe detectors for space and science imaging: general issues and latest achievements. *J. Electron. Mater.* **45**, 4532–4541 (2016).
9. Plis, E. A. InAs/GaSb type-II superlattice detectors. *Adv. Electron.* **2014**, 246769 (2014).
10. Ting, D. Z. et al. InAs/InAsSb type-II strained-layer superlattice infrared photodetectors. *Micromachines* **11**, 958 (2020).
11. Jones, A. H., March, S. D., Bank, S. R. & Campbell, J. C. Low-noise high-temperature AlInAsSb/GaSb avalanche photodiodes for 2-µm applications. *Nat. Photon.* **14**, 559–563 (2020).
12. Maddox, S. J., March, S. D. & Bank, S. R. Broadly tunable AlInAsSb digital alloys grown on GaSb. *Cryst. Growth Des.* **16**, 3582–3586 (2016).
13. Gao, Y. et al. Photon-trapping microstructures enable high-speed high-efficiency silicon photodiodes. *Nat. Photon.* **11**, 301–308 (2017).
14. Song, J. W., Yuan, S., Cui, C. C. & Xia, J. S. High-efficiency normal-incidence germanium photodetector with ultra-thin intrinsic layer. In *Asia Communications and Photonics Conference/International Conference on Information Photonics and Optical Communications 2020 (ACP/IPOC)* M4A.169 (Optica Publishing Group, 2020).
15. Zhou, H. et al. High-efficiency GeSn/Ge multiple-quantum-well photodetectors with photon-trapping microstructures operating at 2 µm. *Opt. Express* **28**, 10280–10293 (2020).
16. Lodari, M. et al. Plasmon-enhanced Ge-based metal-semiconductor-metal photodetector at near-IR wavelengths. *Opt. Express* **27**, 20516–20524 (2019).
17. Latzel, P. et al. Generation of mW level in the 300-GHz band using resonant-cavity-enhanced unitraveling carrier photodiodes. *IEEE Trans. THz Sci. Technol.* **7**, 800–807 (2017).
18. Chen, D. K., Sun, K. Y., Jones, A. H. & Campbell, J. C. Efficient absorption enhancement approaches for AlInAsSb avalanche photodiodes for 2-µm applications. In *2020 IEEE Photonics Conference (IPC)* 1–3 (IEEE, 2020).
19. Shen, J. T., Catrysse, P. B. & Fan, S. H. Mechanism for designing metallic metamaterials with a high index of refraction. *Phys. Rev. Lett.* **94**, 197401 (2005).
20. Hsieh, B. Y. & Jarrahi, M. Analysis of periodic metallic nano-slits for efficient interaction of terahertz and optical waves at nano-scale dimensions. *J. Appl. Phys.* **109**, 084326 (2011).
21. Pendry, J. B., Martin-Moreno, L. & Garcia-Vidal, F. J. Mimicking surface plasmons with structured surfaces. *Science* **305**, 847–848 (2004).
22. Lyaschuk, Y. M. & Korotyeyev, V. V. Interaction of terahertz electromagnetic field with a metallic grating: near-field zone. *Ukr. J. Phys. Opt.* **13**, 142–150 (2012).
23. Mikhailov, S. A. Plasma instability and amplification of electromagnetic waves in low-dimensional electron systems. *Phys. Rev. B* **58**, 1517–1532 (1998).
24. Liu, H. D. et al. Avalanche photodiode punch-through gain determination through excess noise analysis. *J. Appl. Phys.* **106**, 064507 (2009).
25. Mcintyre, R. J. Multiplication noise in uniform avalanche diodes. *IEEE Trans. Electron Devices* **ED-13**, 164–168 (1966).
26. Woodson, M. E. et al. Low-noise AlInAsSb avalanche photodiode. *Appl. Phys. Lett.* **108**, 081102 (2016).
27. Campbell, J. C. Evolution of low-noise avalanche photodetectors. *IEEE J. Sel. Topics Quantum Electron.* **28**, 3800911 (2022).
28. Jones, A. H. et al. Room-temperature bandwidth of 2-µm AlInAsSb avalanche photodiodes. *Opt. Express* **29**, 38939–38945 (2021).
29. Dehzangi, A. et al. High speed antimony-based superlattice photodetectors transferred on sapphire. *Appl. Phys. Express* **12**, 116502 (2019).

Methods

Epitaxial growth

The designed layer structure (Fig. 1b) was grown by molecular-beam epitaxy at 460 °C lattice matched to an n-type GaSb. Solid-source valved crackers provided As$_2$ and Sb fluxes, and solid-source effusion cells provided Al, Ga, In, Be (acceptor) and GaTe (donor) fluxes. The Al$_x$InAsSb layers were grown as digital alloys of stable binaries using a repeating-period shutter sequence: AlSb, AlAs, AlSb, InSb, InAs and Sb soak. Further growth details and optical properties of the resulting material are reported elsewhere[12].

Device fabrication

The wafer was fabricated into circular mesa structures by standard photolithography techniques and citric acid wet etching. Finally, sub-micrometre metal grating arrays were fabricated on top of the mesa by electron-beam lithography and metal lift-off process. It is worth noting that the metal was deposited as a stack of 10 nm Ti and 370 nm Au, where the Ti layer is used to improve adhesion between Au and the semiconductor. A scanning electron microscopy image of the fabricated photon-trapping SACM APD is shown in Fig. 2a. The performance of these APDs is characterized as follows.

Band diagram and electric-field profile simulation

The band structure and electric-field intensity profile of the photon-trapping SACM APD were obtained by Lumerical CHARGE solver. The doping level in the simulation was assumed to be the same as the designed value (Fig. 1b).

Current–voltage characteristics

The current–voltage characteristics were measured with a Keithley 2400 source meter. A 2 μm temperature-stabilized laser coupled to a lensed fibre was used as the optical source. Temperature dependence measurements were performed in a liquid-nitrogen-cooled cryogenic chamber and measured with an HP 4145 semiconductor parameter analyser.

Multiplication gain

Although the punch-through voltage indicates that the charge layer is fully depleted, this does not mean the electric-field magnitude in the multiplication region is at the impact ionization threshold. In fact, the electric field could be above or below this threshold, meaning $M > 1$ or $M = 1$ at the punch-through voltage, respectively. In the former case, there is gain in the multiplication region before punch-through and the true unity-gain point occurs at a slightly lower reverse bias. In the latter case, a higher electric field is required in the multiplication region before impact ionization can occur, meaning that unity gain is at a higher reverse bias than the punch-through voltage. For this reason, the unity-gain point must be determined by another factor that scales with the gain, namely, the excess noise (see the 'Noise power' section). Here the unity-gain point was determined by computationally fitting the measured excess noise to the change in photocurrent using an established method[24]. This methodology results in both best-fit gain and k-factor values.

Capacitance–voltage characteristics

The capacitance–voltage characteristics were measured under blackout conditions with a calibrated HP 4275A LCR meter at 1 MHz to verify the operation voltage of the photon-trapping SACM APD. The depletion width was estimated using the measured capacitance and dielectric constant of AlInAsSb. The charge layer is depleted at almost −16 V where the electric field reaches into the absorber. It is worth noting that the measured punch-through voltage is about 3 V higher than the designed value, which is suspected to be caused by dopant diffusion from the charge layer into the surrounding UID layers.

The capacitance–voltage measurement also indicates that the absorber is not fully depleted right after the punch-through voltage, which is consistent with the analysis for the bandwidth increase before $M \approx 10$, as discussed in the main text.

EQE

The normal-incidence responsivities were measured at punch-through using a high-pressure xenon-gas laser-driven light source, a monochromater and a lock-in amplifier. Photocurrents were normalized to a calibrated strained-layer InGaAs photodiode. For edge-coupled quantum efficiency measurements, a continuous-wave optical input from a temperature-stabilized 2 μm semiconductor laser polarized by a polarization controller was coupled into the device through a lensed fibre. The photoresponse was collected by directly probing the device with a ground–signal–ground probe and the photocurrent was measured with a source meter. The steps for quantum efficiency measurement are described as follows. First, the cleaved device was probed by the ground–signal–ground probe, and the d.c. bias was fixed at the punch-through voltage, that is, −16 V (as discussed in the main text). Then, light was coupled into the edge of the device, whereas the polarization, positions and angles of the lensed fibre were adjusted to provide the highest photocurrent. The lensed fibre was then removed from the device and inserted into an optical power meter with an integrating sphere to measure the input optical power. The responsivity was calculated using the expression $R = \frac{I_{total} - I_{dark}}{P}$, where I_{total} and I_{dark} are the measured total current and dark current, respectively, and P is the measured optical power. The quantum efficiency can be calculated as $\eta = \frac{R \times 1.24}{M \times \lambda}$, where M is the multiplication gain of the device at the measured bias, λ is the wavelength (in μm) and R is the responsivity.

Noise power

The devices were biased with a Keithley 2400 source meter. A 2 μm temperature-stabilized laser coupled to a lensed fibre was used to illuminate the APDs. The a.c. component of the output current was measured with an Agilent 8973A noise figure analyser through a standard radio-frequency bias-tee. Careful system calibration was carried out via a calibrated Agilent 346A noise source to remove the background noise.

Data availability

The data that support the plots within this paper and other findings of this study are available from the corresponding author upon reasonable request.

Author contributions

D.C. carried out the simulations, device fabrication and experimental measurements and authored the paper. S.D.M., A.M.S. and J.A.M. provided the crystal growth and material characterization. A.H.J., Y.S., B.G., A.A.D., K.S. and J.B. assisted with the device measurements and data analysis. X.X. carried out some of the initial device fabrication. J.C.C. and S.R.B. directed the device and materials aspects of the program, respectively.

Competing interests

The authors declare no competing interests.

Additional information